Supplementary Information

Charge-to-spin conversion in twisted graphene/WSe_2 heterostructures

Seungjun Lee,[1,*] D. J. P. de Sousa,[1,*] Young-Kyun Kwon,[2] Fernando de Juan,[3,4] Zhendong Chi,[5] Fèlix Casanova,[5] and Tony Low[1,6,†]

[1]*Department of Electrical and Computer Engineering, University of Minnesota, Minneapolis, Minnesota 55455, USA*

[2]*Department of Physics, Department of Information Display, and Research Institute for Basic Sciences, Kyung Hee University, Seoul, 02447, Korea*

[3]*Donostia International Physics Center, P. Manuel de Lardizabal 4, 20018 Donostia-San Sebastian, Spain*

[4]*IKERBASQUE, Basque Foundation for Science, Maria Diaz de Haro 3, 48013 Bilbao, Spain*

[5]*CIC nanoGUNE, 20018, Donostia-San Sebastián, Basque Country, Spain*

[6]*Department of Physics, University of Minnesota, Minneapolis, Minnesota 55455, USA*

(Dated: September 12, 2022)

Note S1: Computational details

We performed first-principles calculations based on density functional theory (DFT)[S1] as implemented in Vienna *ab initio* simulation package (VASP)[S2]. The exchange-correlation (XC) functional was treated within the generalized gradient approximation of Perdew-Burke-Ernzerhof (PBE)[S3] with noncollinear spin polarization.[S4] The electronic wavefunctions were expanded by planewave basis with kinetic energy cutoff of 400 eV. We employed the projector-augmented wave pseudopotentials[S5,S6] to describe the valence electrons, and Grimme-D2 van der Waals correction[S7] to describe long range interaction between graphene and WSe_2. The sufficiently large vacuum region was included to mimic 2D layered or slab structure in periodic cells.

To construct supercell configurations with various twist angles, we employed accidental angular commensuration method.[S8,S9] In the hexagonal two-dimensional materials, any supercell structrue (m, n) can be defined by two lattice vectors $\mathbf{a}_{(\mathrm{m,n})} = m\mathbf{a} + n\mathbf{b}$ and $\mathbf{b}_{(\mathrm{m,n})} = -m\mathbf{a} + (m+n)\mathbf{b}$ with a corresponding skewed angle $\theta_{(\mathrm{m,n})} = tan^{-1}(\sqrt{3}m/(2n+m))$. Based on the equilibrium lattice constants of graphene ($a^{\mathrm{Gra}} = 2.46$ Å) and WSe_2 ($a^{\mathrm{WSe_2}} = 3.32$ Å), we constructed supercells of graphene (m, n) and WSe_2 (m', n'), and stacked them to make heterostructures while keeping their lattice mismatch below 2%. The twist angle is obtained by $\theta = |\theta^{\mathrm{Gra}}_{(\mathrm{m,n})} - \theta^{\mathrm{WSe_2}}_{(\mathrm{m',n'})}|$, and the lattice constants of heterostructure was used to be the same value as $a^{\mathrm{Gra}}_{(\mathrm{m,n})}$. Within the given lattice constants, the atomic positions were fully relaxed through DFT calculation. The detailed structural parameters and corresponding k-mesh gird ($N_k \times N_k$) of the heterostructures are summarized in Table S1.

The band (n) and momentum ($\mathbf{k}$) resolved spin angular momentum distributions are calculated by the expectation value of the spin angular momentum operator, that is, $\sum_\alpha \langle \psi^\alpha_{n,\mathbf{k}} | \boldsymbol{\sigma} | \psi^\alpha_{n,\mathbf{k}} \rangle$, where $\boldsymbol{\sigma}$ is the Pauli spin matrix vector, and $\psi^\alpha_{n,\mathbf{k}}$ is an wavefunction projected on atom site α.

Note S2: Quantum transport calculation details

The quantum transport calculations are based on a periodic tight-binding model for the proximitized graphene Dirac states. The Hamiltonian reads[S10]

$$
\begin{aligned}
H = & \sum_{\langle ij\rangle,\sigma} \hat{c}^{\dagger}_{i\sigma} t \hat{c}_{j\sigma} + \sum_{i,\sigma} \hat{c}^{\dagger}_{i\sigma} \Delta \xi_{c_i} \hat{c}_{i\sigma} + \\
& \frac{2i\lambda_{\mathrm{R}}}{3} \sum_{\langle ij\rangle,\sigma\sigma'} \hat{c}^{\dagger}_{i\sigma} [e^{-i\hat{s}_z\phi/2} (\hat{\mathbf{s}} \times \hat{\mathbf{d}}_{ij}) \cdot \hat{\mathbf{z}} e^{i\hat{s}_z\phi/2}]_{\sigma\sigma'} \hat{c}_{j\sigma} \\
& + \frac{i}{3} \sum_{\langle\langle ij\rangle\rangle,\sigma\sigma'} \hat{c}^{\dagger}_{i\sigma} \left[\frac{\lambda_I^{c_i}}{\sqrt{3}} \nu_{ij} s_z + 2\lambda_{\mathrm{PIA}}^{c_i} (\hat{\mathbf{s}} \times \hat{\mathbf{D}}_{ij}) \cdot \hat{\mathbf{z}} \right]_{\sigma\sigma'} \hat{c}_{j\sigma},
\end{aligned}
\tag{S1}
$$

where $\hat{c}^{\dagger}_{i\sigma}$ ($\hat{c}_{i\sigma}$) creates (annihilates) a p_z electron with spin σ at site i, t is the nearest neighbor hopping parameter and Δ is the sublattice asymmetry with $\xi_{A(B)} = \pm 1$. The remaining parameters λ_{R}, $\lambda_{\mathrm{I}}^{\mathrm{A,B}}$ and $\lambda_{\mathrm{PIA}}^{\mathrm{A,B}}$ collectively account for the proximity-induced SOC and describe, respectively, the Rashba SOC, the sublattice resolved intrinsic SOC and pseudospin inversion asymmetry induced terms. In addition $\nu_{ij} = +1(-1)$ describes the relative phase acquired by an electron as it travels from sites i and j in a clockwise (counterclockwise) sense and $\hat{d}_{ij}$ and $\hat{D}_{ij}$ are, respectively, the nearest neighbor and next-nearest neighbor unit vectors connecting sites i and j. Finally, $\hat{s}$ is the vector of spin Pauli matrices and ϕ is the Rashba angle parameter accounting for the non-orthogonal spin-momentum locking[S11–S14]. The above Hamiltonian can be Fourier transformed to momentum space, from where eigenstates and energy bands relevant for the linear response formula are obtained.

Figure S5 displays the energy dependence of the spin Hall conductivity and Rashba-Edelstein efficiency (up to a factor of v_F) for all twist angles considered in this work. From Fig. S5(a) it is clear that the spin Hall conductivity is maximized at 30° twisting at all energies. This implies that the Rashba-like spin texture in this situation is beneficial to the spin Hall effect. The Rashba-Edelstein efficiency in Fig. S5(b) shows that the maximum efficiency varies with energy, where maximum efficiency occurs at the vicinity of 30° twisting at low doping levels.

Figure S6 is a study on the relevance of the proximity-induced pseudospin inversion asymmetry on the charge-to-spin conversion. We considered two situations, where we artificially set $\lambda_{\mathrm{PIA}}^{A,B}$ to zero or maintained its value to that obtained by fitting the first-principles ground states. Panels (a) and (b) show that the same behavior is expected regardless of the $\lambda_{\mathrm{PIA}}^{A,B}$ we

assume. The same conclusion is valid for all twist angles we considered (two sample twist angle cases are shown). Hence, the pseudospin inversion asymmetry SOC due to procimity-effects is not relevant to charge-to-spin conversion in Gra/TMDC heterostructures.

Figure S7 is a sample calculation showing that the valley Zeeman SOC parameter is detrimental to the charge-to-spin conversion efficiencies. In these calculations, we artificially increase the absolute values of the parameters $\lambda_I^{A,B}$ while maintaining the remaining parameters fixed at those corresponding to the 0° twisted structure. As is seen, the maximum efficiency decays and is shifted to higher energies at larger λ_{VZ} for both spin Hall and Rashba-Edelstein effects. The energy shift is due to the band structure modification associated with $\lambda_I^{A,B}$, while the suppression is mainly due to the larger longitudinal conductivity σ_{xx} at larger λ_{VZ}. It is worth emphasizing that these results are valid in the weak disorder limit, where the constant Γ approximation provides a good description. In the strong disorder limit, the relation between efficiency and valley-Zeeman SOC is qualitatively distinct.

Note S3: Crossover of Spin Hall and Rashba-Edelstein dominated charge-to-spin conversion: A illustrative calculation.

As pointed out in the main text, although vertex corrections are fundamentally necessary to fully address the SHE in proximitized-graphene, we compute the twisted angle dependence of the disorder-free spin Hall conductivity as a reference for future calculations including disorder. In this spirit, we also find it useful to analyse the crossover between the SHE and (U)REE dominated CSC with spectral broadening, twist angle and doping levels, which is presented in this section for illustration purposes.

To facilitate this study we define a CSC efficiency polarization as $\xi(E,\theta) = (|\theta_{\rm SHE}| - |\alpha|)/(|\theta_{\rm SHE}| + |\alpha|)$ where $\alpha = \sqrt{\alpha_{\rm REE}^2 + \alpha_{\rm UREE}^2}$, and tracked its evolution with the band broadening Γ in Fig. S8. For small band broadening ($\Gamma = 0.1$ meV), ξ is mostly negative for all energies and twist angles, i.e., CSC is dominated by the REEs [See Fig. S8(a)]. At large spectral broadening ($\Gamma = 0.50$ meV), ξ turned positive throughout, as shown in Fig. S8(c), indicating that SHE dominates the CSC. We identify an intermediate crossover broadening ($\Gamma = 0.25$ meV), the dominating mechanism for CSC strongly depends on the twist angle and doping levels, being mostly due to SHE close to 30° twisting and to REE at higher doping levels for twist angles in the interval $5° - 25°$, as shown in Fig. S8(b). The strong Γ

dependence of ξ originates from the contrasting Fermi sea and Fermi surface nature of SHE and REEs, respectively. Here, $\delta s^{x,y}$ and σ_{xx} are both Fermi surface effects, such that their dependences on Γ compensate and give rise to an α that is approximately independent of Γ. On the contrary, the SHE is approximately independent of Γ because it originates from the Fermi sea. Hence, σ_{yx}^{z} does not compensate the Γ dependence of σ_{xx}. These findings shed light on the disparate dominant CSC mechanism reported across different proximitized graphene Hall bar devices and might help guiding future work in this direction.

TABLE S1. Structural parameters of the twisted graphene/WSe_2 heterostructure. The lattice constants of heterostructure was used to be the same value as $a^{\mathrm{Gra}}_{(\mathrm{m,n})}$, and the residual strain was only applied to the WSe_2 (m', n').

θ (°)	Strain (%)	N_k	$a^{\mathrm{Gra}}_{(\mathrm{m,n})}$	m	n	$\theta^{\mathrm{Gra}}_{(\mathrm{m,n})}$	$a^{\mathrm{WSe_2}}_{(\mathrm{m',n'})}$	m'	n'	$\theta^{\mathrm{WSe_2}}_{(\mathrm{m',n'})}$
0.00	1.20	6	9.84	4	0	0.00	9.96	3	0	0.00
5.21	-0.98	3	15.36	5	2	16.10	15.21	4	1	10.89
13.07	0.29	2	20.14	7	2	12.22	20.19	4	3	25.29
16.58	-0.98	2	23.47	9	1	5.21	23.24	5	3	21.79
19.11	-1.98	4	13.02	4	2	19.11	13.28	4	0	0
23.41	2.00	4	14.76	6	0	0	14.47	3	2	23.41
27.00	-0.98	2	23.47	6	5	27.00	23.24	7	0	0.00
30.00	0.18	2	17.22	7	0	0.00	17.25	3	3	30.00

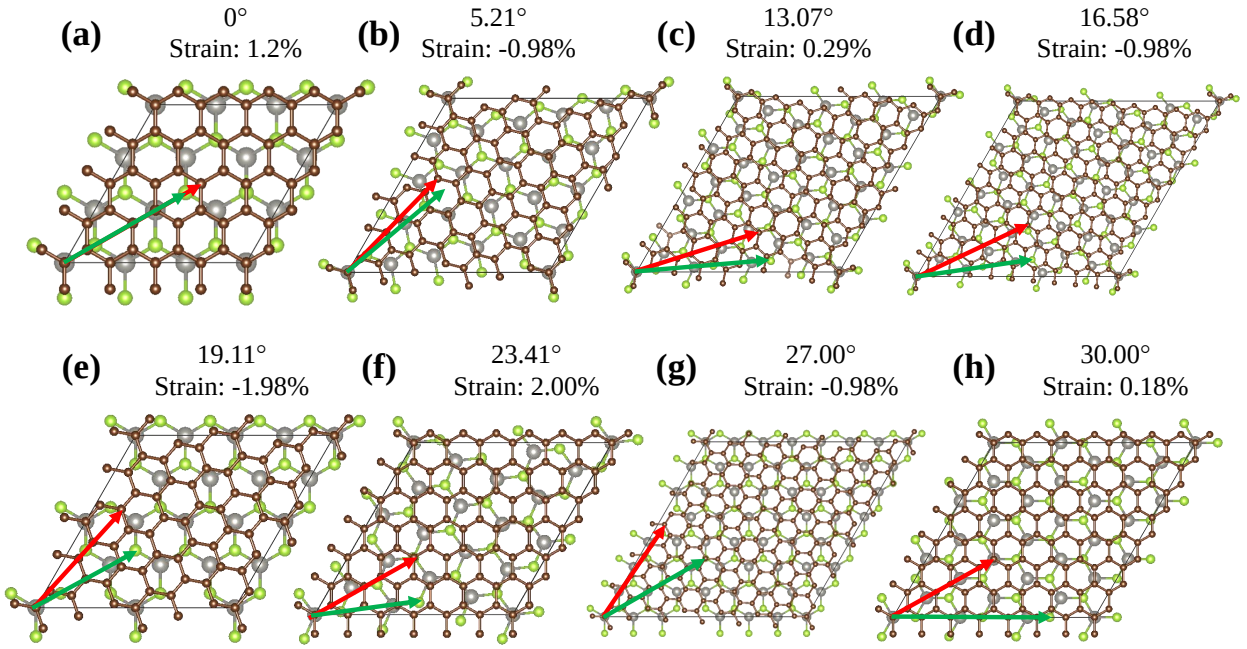

FIG. S1. (a–h) Crystal structure of twisted graphene/WSe_2 heterostructures with a total of 8 twist angles. Brown, grey, and green spheres indicate carbon, tungsten, and selenium atoms, respectively. In each figure, red and green arrows show the armchair directions of graphene and WSe_2.

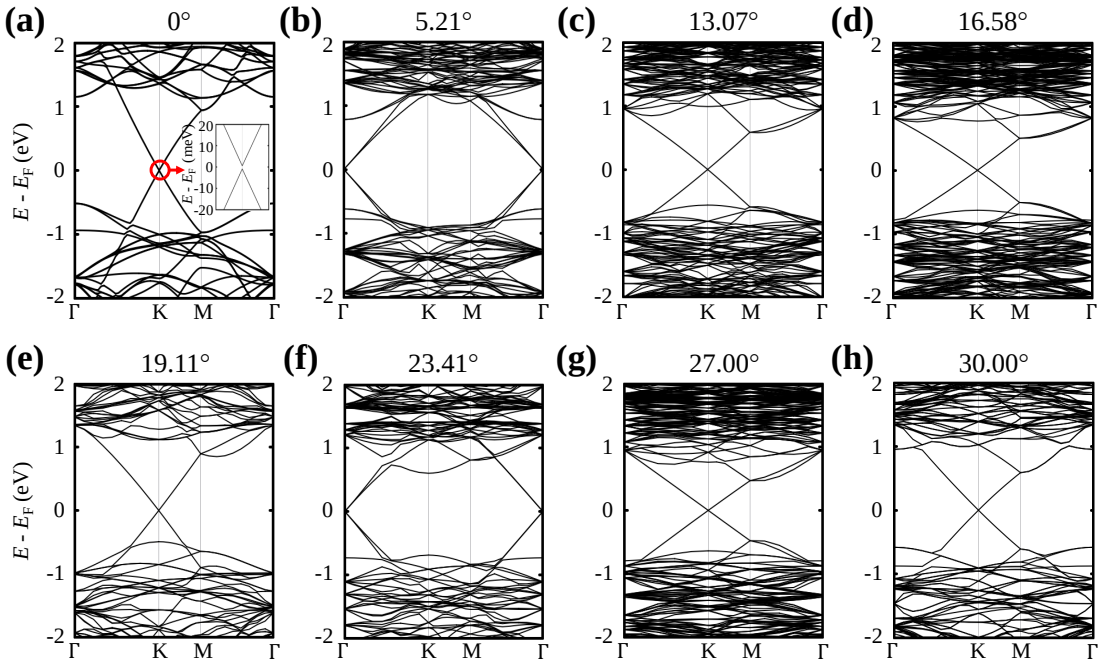

FIG. S2. (a–h) Electronic structure of twisted graphene/WSe_2 heterostructures without spin-orbit interaction. In (a), inset shows small band gap opening at the Dirac point.

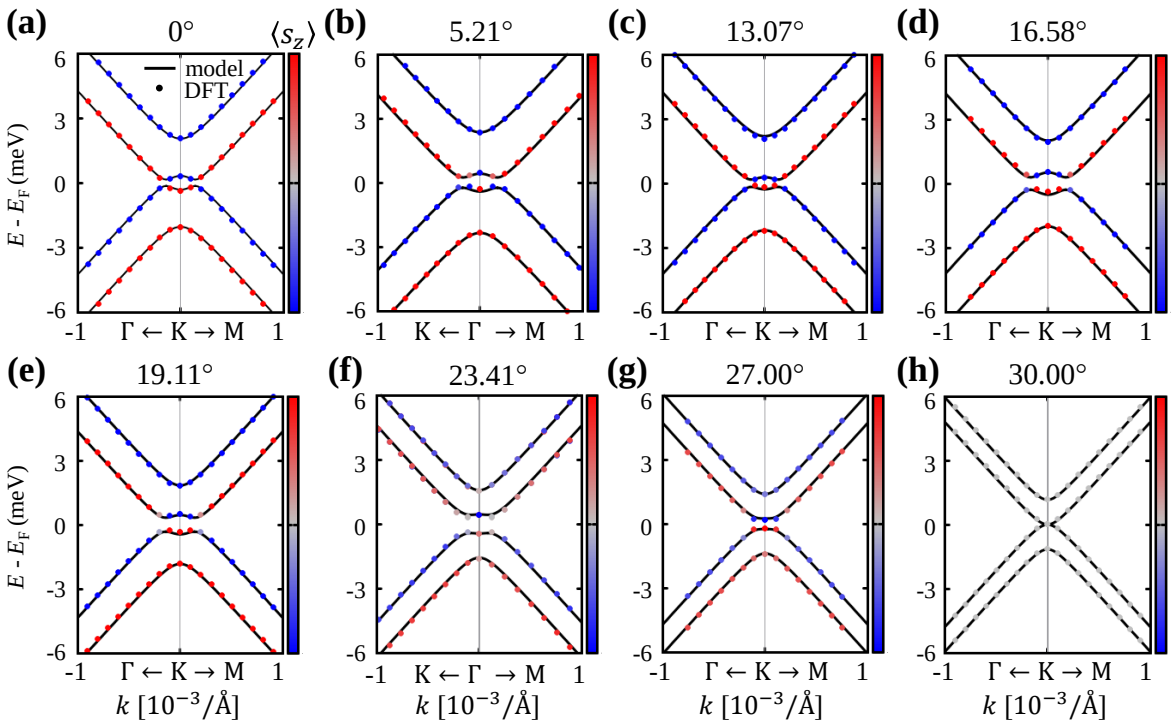

FIG. S3. (a–h) Spin-orbit proximitized carbon p_z states of twisted graphene/WSe_2 heterostructures. The colored dots show the energy eigenvalues calculated by DFT, which were fitted by the model defined as the Eq. (1) in the main manuscript, plotted with black solid lines. In (a), colorbox indicates expectation value of out-of-plane spin components.

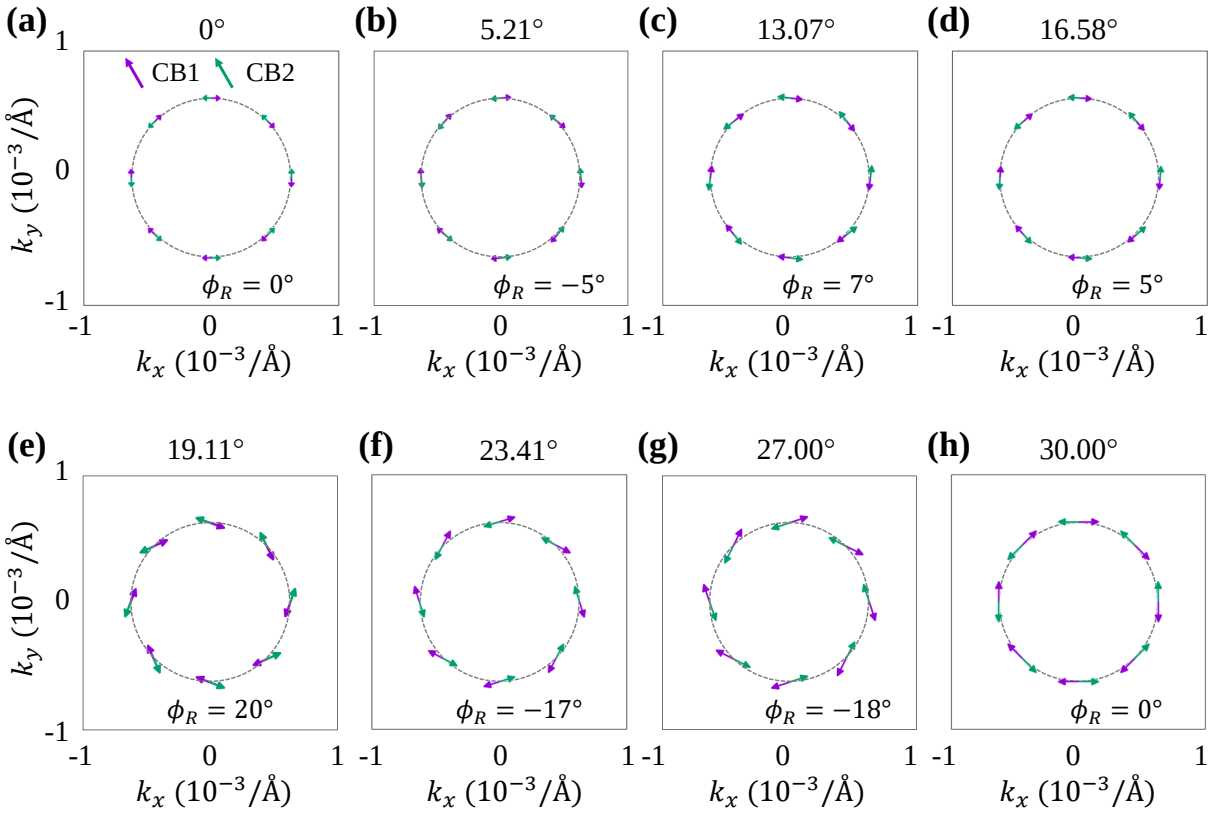

FIG. S4. (a–h) In-plane spin angular momentum distributions of the heterostructures with twist angles from 0° to 30°. The purple and cyan arrows indicate the (CB1) lowest and (CB2) second lowest conduction bands (two upper Dirac bands) with opposite spin-chiralities. The lowest and second highest valence bands (two lower Dirac bands) have exactly the same spin-chiralities with those of the CB1 and CB2, respectivley. In each figure, we represented Rashba phase angle ϕ_R, which induces deviations from the ideal spin-momentum locking (highlighted by dashed circles).

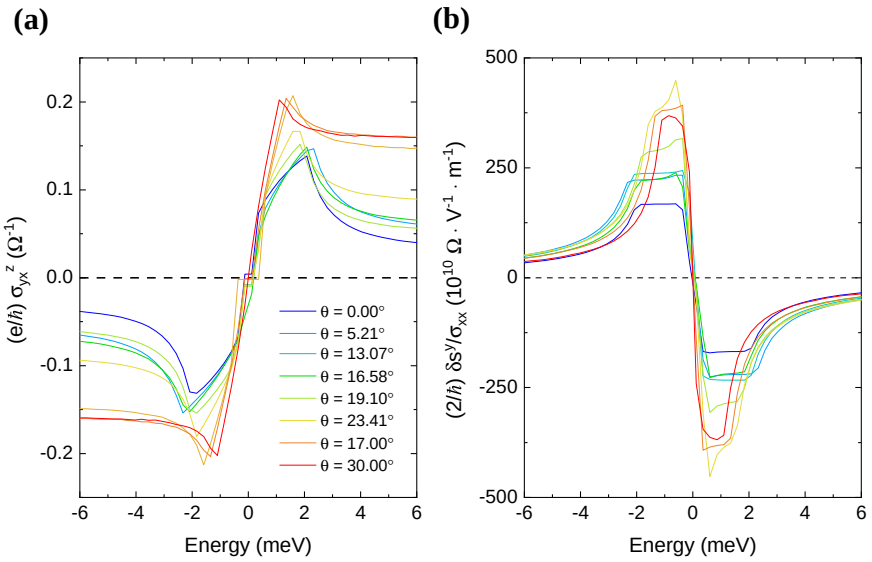

FIG. S5. Energy resolved (a) spin Hall conductivity and (b) Rashba-Edelstein efficiency at several twist angles.

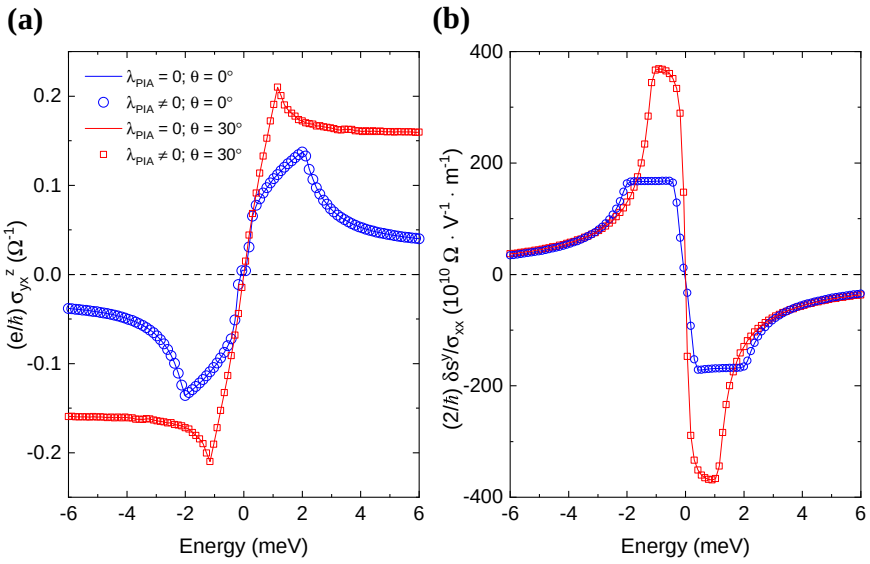

FIG. S6. Dependence of the (a) spin Hall conductivity and (b) Rashba-Edelstein efficiency with the pseudospin inversion asymmetry parameters $\lambda_{\mathrm{PIA}}^{A,B}$, represented collectively as λ_{PIA}, at two sample twist angles. Here, $\lambda_{\mathrm{PIA}} \neq 0$ means the calculation was performed with full $\lambda_{\mathrm{PIA}}^{A,B}$ value as fitted from first-principles.

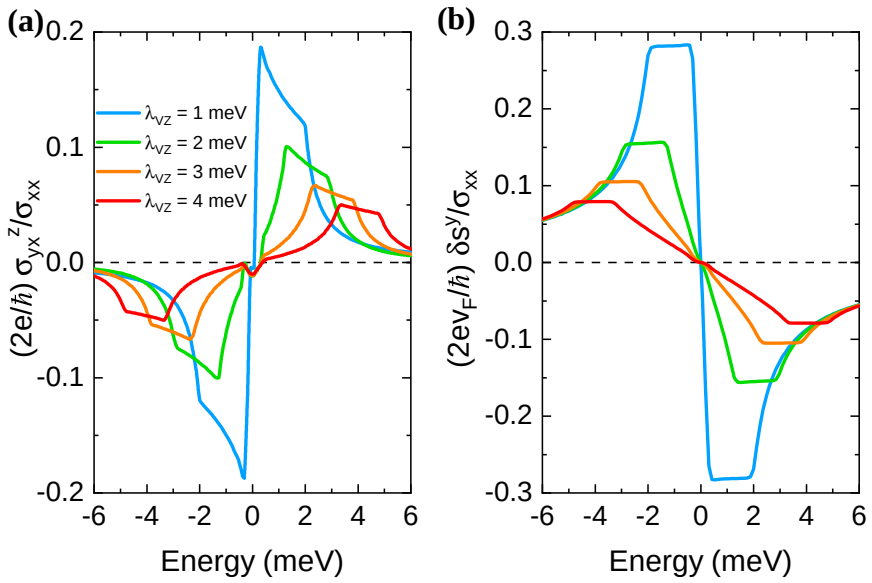

FIG. S7. Evolution of spin Hall and Rashba-Edelstein efficiencies with the valley Zeeman parameter. Here, all remaining parameters are fixed and assumed to coincide with those of the 0° twisted structure.

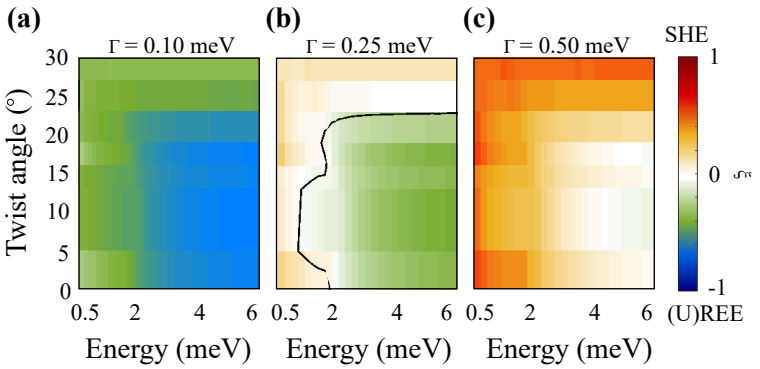

FIG. S8. Evolution of the CSC diagram with the band broadening: (a) $\Gamma = 0.10$ meV, (b) $\Gamma = 0.25$ meV and (c) $\Gamma = 0.50$ meV. Here, $\xi(E,\theta) = (|\theta_{\rm SHE}| - |\alpha|)/(|\theta_{\rm SHE}| + |\alpha|)$ is a CSC efficiency polarization, where $\alpha = \sqrt{\alpha^2_{\rm REE} + \alpha^2_{\rm UREE}}$, such that stronger positive (negative) regions imply in dominant CSC through SHE (REE or UREE). The contour in panel (b) separates dominating SHE and REE/UREE scenarios where $\xi = 0$.

---

* These authors contributed equally to this work.

† tlow@umn.edu

[S1] W. Kohn and L. J. Sham, Phys. Rev. **140**, A1133 (1965).

[S2] G. Kresse and J. Furthmüller, Phys. Rev. B **54**, 11169 (1996).

[S3] J. P. Perdew, K. Burke, and M. Ernzerhof, Phys. Rev. Lett. **77**, 3865 (1996).

[S4] S. Steiner, S. Khmelevskyi, M. Marsmann, and G. Kresse, Phys. Rev. B **93**, 224425 (2016).

[S5] P. E. Blöchl, Phys. Rev. B **50**, 17953 (1994).

[S6] G. Kresse and D. Joubert, Phys. Rev. B **59**, 1758 (1999).

[S7] S. Grimme, J. Comput. Chem. **27**, 1787 (2006).

[S8] Z. Wang, Q. Chen, and J. Wang, J. Phys. Chem. C **119**, 4752 (2015).

[S9] A. N. Kolmogorov and V. H. Crespi, Phys. Rev. B **71**, 235415 (2005).

[S10] D. Kochan, S. Irmer, and J. Fabian, Phys. Rev. B **95**, 165415 (2017).

[S11] Y. Li and M. Koshino, Phys. Rev. B **99**, 075438 (2019).

[S12] A. David, P. Rakyta, A. Kormányos, and G. Burkard, Phys. Rev. B **100**, 085412 (2019).

[S13] T. Naimer, K. Zollner, M. Gmitra, and J. Fabian, Phys. Rev. B **104**, 195156 (2021).

[S14] A. Pezo, Z. Zanolli, N. Wittemeier, P. Ordejón, A. Fazzio, S. Roche, and J. H. Garcia, 2D

Mater. **9**, 015008 (2021).